On dark stars, galactic rotation curves and fast radio bursts

On dark stars, galactic rotation curves and fast radio bursts

Igor Nikitin

Fraunhofer Institute for Algorithms and Scientific Computing,
Schloss Birlinghoven, 53757 Sankt Augustin, Germany

E-mail: igor.nikitin@scai.fraunhofer.de

Abstract. This paper is a continuation of our recent work on Radial Dark Matter stars (RDM-stars), black holes, coupled with radial flows of dark matter. As a galaxy model, it produces flat rotation curves, approximately valid for many galaxies far from the center. In this paper, more detailed modeling is carried out, including the vicinity of the galactic center. Assuming that the distribution of stellar black holes repeats the distribution of luminous matter, we get a perfect match between the model rotation curves and the observed ones. Further, using numerical integration, we examine the gravitational field of an individual RDM-star. The computation shows the event horizon being erased and rapidly increasing mass density arising instead (mass inflation). In this regime, we apply the previously constructed Planck star model, where at high densities a repulsive force occurs (quantum bounce). In our stationary model, the evolution of a Planck star has stopped under the pressure of dark matter flows. This system is considered as a possible source of Fast Radio Bursts (FRBs). In a scenario involving an asteroid falling onto an RDM-star, the model reproduces the correct frequency range of FRBs. Their total energy, coherence and short duration are explained as well.

1. Introduction

This paper continues our work [1] studying the model of Radial Dark Matter stars (RDM-stars). These solutions belong to a recently proposed class of *dark stars* or *quasi-black holes*, solutions closely following Schwarzschild's profile outside the gravitational radius and behaving completely different under it. Known solutions of this class include quark stars, strange stars, boson stars, gravastars, fuzzballs, their review can be found in [2].

The geometry of an RDM-star is shown on Fig. 1. It is a stationary solution composed of radially converging and radially diverging dark matter flows. An RDM-star emits dark matter and also absorbs it in equal amounts, so that the masses enclosed by r-spheres conserve in time. This geometry possesses $\rho \sim r^{-2}$ dependence for the mass density, linear for the enclosed mass $M \sim r$ and constant for the orbital velocity $v^2 = GM/r = Const$. As a result, an RDM-star can be used to model the distribution of dark matter in spiral galaxies. Being placed to the center of a galaxy, it produces the flat shape of rotation curves, typical for many galaxies at large distance from the center. In this work we will consider more detailed modeling of the rotation curves, valid also in the vicinity of the galactic center. The idea is to consider not only the central supermassive, but also all stellar black holes as RDM-stars. Assuming that the distribution of stellar black holes repeats the distribution of stars in the galaxy, we are able to compute the dark matter distribution and the resulting correction to the rotation curves.

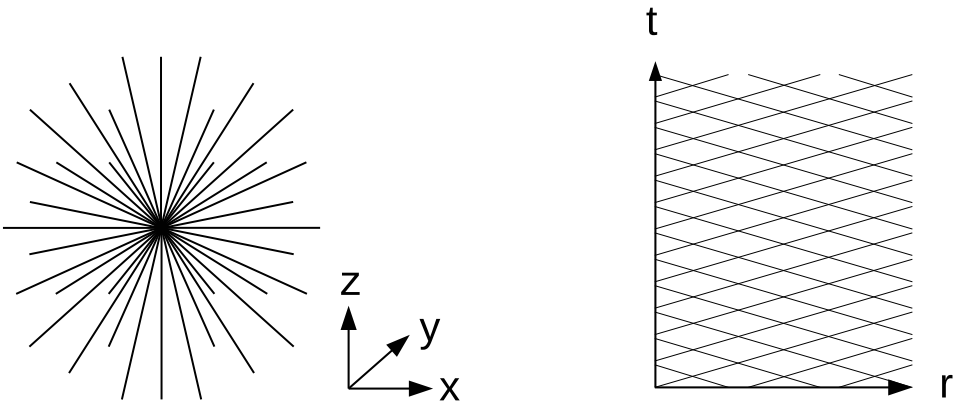

Figure 1. RDM-star: a black hole, coupled to radial flows of dark matter, in xyz and tr coordinates. Image from [1].

Since the pioneering works of Rubin et al. in 1970s [3, 4], the rotation curves have been considered as the indicators of dark matter in galaxies. Basically, there is a large excess of mass necessary to explain the observed orbital velocities, which cannot be associated with the stars and the interstellar gas in the galaxies. The nature of this hidden mass, the dark matter is still unknown. There are many proposals including new types of elementary particles: massive neutrinos, axions, WIMPs, WISPs, see [5] for the review. The models considered in this paper do not depend on the composition of dark matter and describe only its spatial distribution.

There are two types of rotation curves used as phenomenological description of the astronomical observations. The *Universal Rotation Curve* (URC, [6–10]) describes the averaged orbital velocities of all the observed spiral galaxies by a single function of distance and luminosity. The *Grand Rotation Curve* (GRC, [11–14]) is the high resolution rotation curve of the Milky Way galaxy, covering the range of distances 1.1pc-1.6Mpc, from the central supermassive black hole to the intergalactic space. In Sections 2,3 we will perform a fit of these two curves by the RDM-star model, resulting in a very good match between the model and the observations.

Further, we will consider the RDM-star model in the regime of strong gravitational field. Here the crossing matter streams lead to the known phenomenon of *mass inflation* [15]. The consequence of this phenomenon is the erasing of the event horizon, which is replaced by a region of super-strong gravitational redshift and a rapidly increasing mass density. When the density exceeds the Planck values, the model of *Planck star* [16, 17] can be applied. According to this model, in gravitational collapse of the stars, after exceeding the Planck density, the gravitational force becomes repulsive and the collapse is changed to a quantum bounce. We will consider a stationary version of this model, where a Planck core is formed inside the RDM-star, with the repulsive force stabilized by the pressure of the dark matter flows. This system will be considered as a possible source of *Fast Radio Bursts* (FRBs).

FRBs are superpowerful flashes observed in the radio band, whose nature currently is a puzzle to astrophysicists. The parameters of registered bursts are cataloged by FRBCAT (http://frbcat.org, [18]), there is also a live catalogue for the existing theories FRBTHEORYCAT (https://frbtheorycat.org, [19]). At the time of writing this paper, 111 FRB sources were detected and 59 FRB theories were constructed. In these theories, the FRBs have been connected to gamma-ray bursts, hyperflares of magnetars, collapse of pulsars, superradiance, cosmic masers, axion miniclusters, cosmic strings, even to extraterrestrial intelligence. We contribute to this field by creating a model of FRB, where an asteroid falls onto the Planck core of an RDM-star and produces a flash of ultra-high energy photons. Then the super-strong gravitational redshift

moves the frequency of these photons to the radio diapason. The formula for the resulting photon frequency can be derived which does not contain freely adjustable parameters and points in the middle of the observed range of FRB frequencies. This computation and the analysis of other characteristics of FRBs is performed in Section 4 of the given paper. Section 5 combines the analysis of RCs and FRBs in frames of the RDM-star model.

Three appendices contain the necessary technical details of the constructions.

2. RDM-stars and URC

In the papers by Kirillov [20–23], Kirillov and Turaev [24, 25] a model of the universal coupling between dark and luminous matter has been developed, in a form of the integral (further referred as *KT-integral*):

$$\rho_{dm}(x) = \int d^3x'\, b(x,x')\, \rho_{lm}(x'), \tag{1}$$

where ρ_{lm} is the mass density of luminous matter, ρ_{dm} is the mass density of dark matter. Due to the symmetries, the kernel can be written in a form $b(x,x') = b(|x-x'|)$, with the following proposed dependence on the distance:

$$b(r) = 1/(4\pi L_{KT})/r^2, \tag{2}$$

where L_{KT} is a constant of the dimension of length. The physical interpretation of this formula is that each mass element of the luminous matter $M_{lm} = (d^3x\, \rho_{lm})$ corresponds to a spherically symmetric distribution of dark matter with density and enclosed mass function of the form

$$\rho_{dm}(r) = M_{lm}/(4\pi L_{KT})/r^2, \tag{3}$$

$$M_{dm}(r) = 4\pi \int_0^r dr' r'^2 \rho_{dm}(r') = M_{lm} r/L_{KT}. \tag{4}$$

That is, the enclosed dark matter mass depends on the distance linearly and L_{KT} determines the slope of this dependence. Specifically, this is the distance at which the mass of dark matter equals to the mass of the luminous matter, to which it is coupled, $M_{dm}(L_{KT}) = M_{lm}$. The contribution of dark matter to the orbital acceleration, orbital velocity and gravitational potential is:

$$a_{r,dm} = GM_{dm}(r)/r^2 = GM_{lm}/(rL_{KT}), \tag{5}$$

$$v_{dm}^2 = GM_{dm}(r)/r = GM_{lm}/L_{KT}, \tag{6}$$

$$\varphi_{dm} = GM_{lm}/L_{KT} \cdot \log r. \tag{7}$$

From here we see that for a point source or at large distances from a compact mass distribution, asymptotically flat rotation curves $v_{dm} = Const$ are reproduced.

In our paper [1] a model of a black hole, coupled to radial flows of dark matter, *an RDM-star*, has been constructed. Due to its geometry with radially divergent flows, see Fig.1, the RDM-star possesses the dark matter density profile $\rho_{dm} \sim r^{-2}$ identical with the kernel of KT-integral. While a single RDM-star produces the flat rotation curve, the distribution of RDM-stars in the galaxy modulates this dependence, generally producing the non-flat curve. If we assume that all black holes are RDM-stars and the density of black holes in the galaxy is proportional to the density of the luminous matter: $\rho_{bh} \sim \rho_{lm}$, then the distribution of the dark matter will be described by KT-integral (1-2) with all the resulting formulae (3-7). In this and the next sections we will compute this integral for the available galactic models (URC and GRC) and compare the resulting rotation curves with the experimental data.

URC is based on *Freeman's exponential disk model* [26], describing the surface mass density of luminous matter by an exponential function $\Sigma_{lm}(r) \sim \exp(-r/R_D)$. In Appendix A we compute KT-integral for this distribution, which together with the formulae [8, 26] for luminous matter produces the following model:

$$v^2_{center,lm} = \alpha_0 v^2_{opt} R_{opt}/r,\ v^2_{center,dm} = \alpha v^2_{opt},\ v^2_{disk,lm} = \beta v^2_{opt} F_{disk}(r/R_D)/F_{disk}(3.2), \quad (8)$$

$$v^2_{disk,dm} = \gamma v^2_{opt} F_{disk,dm}(r/R_D)/F_{disk,dm}(3.2),\ R_{opt} = 3.2R_D,\ v^2_{opt} = v^2(r \to R_{opt}), \quad (9)$$

$$F_{disk}(x) = x^2(I_0(x/2)K_0(x/2) - I_1(x/2)K_1(x/2)),\ F_{disk,dm}(x) = 1 - e^{-x}(1+x), \quad (10)$$

$$v^2 = v^2_{center,lm} + v^2_{center,dm} + v^2_{disk,lm} + v^2_{disk,dm},\ \alpha_0 + \alpha + \beta + \gamma = 1, \quad (11)$$

where I_n, K_n are the modified Bessel functions. We took into account the contribution of the galactic center, including the central supermassive black hole and the bulge. At the considered range of distances it is represented by an unresolved point-like contribution and is described by the asymptotic compact mass formulae above. The velocities are normalized to R_{opt} distance, under which 83% of the luminous mass is located. The coefficients in the additive formulae for squared velocities become the parameters for fitting the model to the experimental data.

The data [6] represent the rotation curves of 967 spiral galaxies, normalized to r/R_{opt} and v/v_{opt}, averaged in 10 luminosity bins. The same data have been used later in [7] to evaluate the dark matter contribution. Then in [8] they have been extended by an additional dataset and the behavior of the rotation curve in the range $1 \le r/R_{opt} \le 2$ has been estimated. Further, in [9] even larger distances have been considered. In this section we restrict our analysis to the original [6] dataset with the range $0.1 \le r/R_{opt} \le 1.2$ and discuss the modeling of larger distances in the next section.

The experimental data are shown in Fig.2 by blue points with error bars. We see that the model, represented by green lines, fits the data perfectly. On the right part of Fig.2 we plot the same data in velocity squared coordinate and show the separated contributions of luminous matter (red) and dark matter (blue). The dark matter central and disk contributions on this plot are added together: $v^2_{dm}(r) = v^2_{center,dm} + v^2_{disk,dm}(r)$. On necessity they can be separated back with the formulas $v^2_{center,dm} = v^2_{dm}(0)$, $v^2_{disk,dm}(r) = v^2_{dm}(r) - v^2_{dm}(0)$. The central luminous matter contribution $v^2_{center,lm} \sim \alpha_0$ is comparable with zero, according to our fit. This means that Keplerian contribution of the galactic center to the orbital velocities of stars is negligible at the distances resolved by URC.

Considering this plot further, for small luminosity ($mag = -18.29$) dark matter describes the experimental rotation curves dominantly, with a negligible luminous matter contribution. Then, with increasing luminosity, the contribution of dark matter diminishes, while the contribution of luminous matter increases. For higher luminosity ($mag = -23.08$) the contribution of luminous matter starts to prevail at intermediate distances, while at large distances the dark matter dominates always. This behavior qualitatively coincides with [8]. The difference is the other form of dark matter term:

$$v^2_{disk,dm} \sim (r/R_{opt})^2/((r/R_{opt})^2 + a^2), \quad (12)$$

which represents an empirical *cored* dark matter distribution with the core radius a becoming in [8] a function of luminosity. Such velocity distribution is produced by a spherically symmetric halo with a bounded density in the center $\rho_{sph}(0) < C$ and enclosed mass function $M_{sph}(r) \sim r^3$, so that the squared velocity becomes $v^2_{sph} = GM_{lm}(r)/r \sim r^2$. Note that in our model the dark matter disk contribution has the same behavior. Specifically, the dark matter contribution $v^2_{disk,dm} = GM_{lm}(r)/L_{KT}$ is proportional to the planar enclosed mass function $M_{lm}(r) \sim r^2$ and possesses the same $r \to 0$ asymptotics as v^2_{sph}.

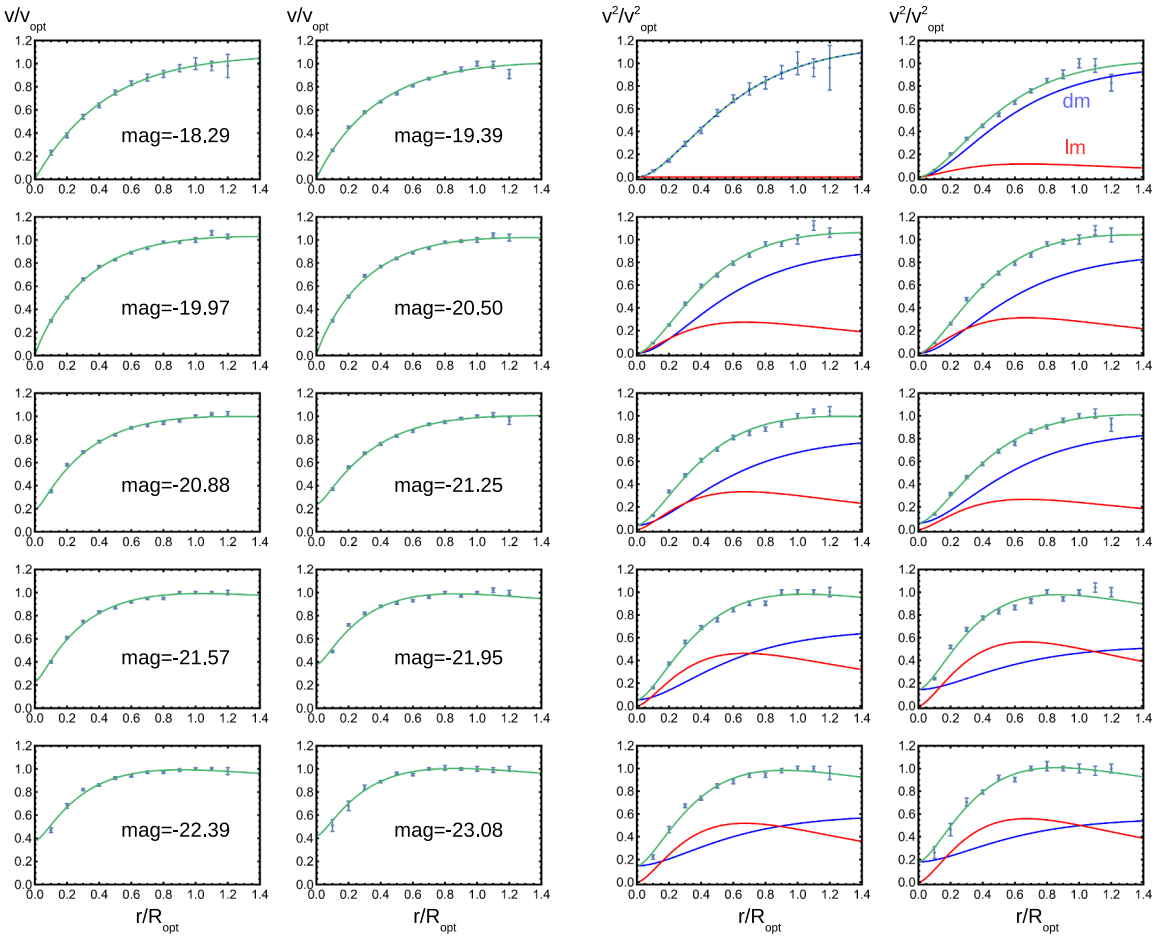

Figure 2. RDM model fits the URC. The points are experimental data from [6], the curves are the fit with RDM model. The left two columns show the dependence of v/v_{opt} on r/R_{opt} for different luminosity bins *mag*. The right two columns show the same plots in velocity squared coordinate. The contributions of luminous matter (red) and dark matter (blue) are separated. The green line is the sum of these contributions.

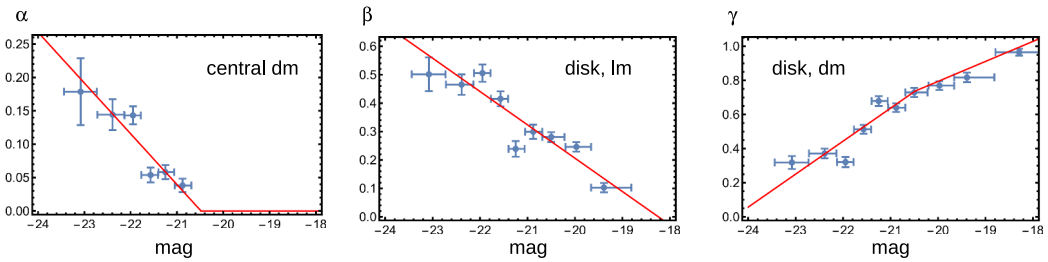

Figure 3. The fit of α, β, γ coefficients as functions of the magnitude. The contributions of central dark matter, disk luminous matter and disk dark matter are separated.

Table 1. URC fitting results

mag	α, central dm	β, disk lm	γ, disk dm
-18.29	0	0	0.965 ± 0.020
-19.39	0	0.103 ± 0.016	0.817 ± 0.028
-19.97	0	0.246 ± 0.017	0.770 ± 0.026
-20.5	0	0.281 ± 0.017	0.729 ± 0.027
-20.88	0.038 ± 0.010	0.299 ± 0.025	0.640 ± 0.025
-21.25	0.058 ± 0.011	0.239 ± 0.027	0.679 ± 0.029
-21.57	0.054 ± 0.011	0.415 ± 0.026	0.513 ± 0.026
-21.95	0.143 ± 0.013	0.505 ± 0.030	0.321 ± 0.030
-22.39	0.144 ± 0.023	0.465 ± 0.036	0.371 ± 0.028
-23.08	0.179 ± 0.050	0.501 ± 0.059	0.319 ± 0.038

Table 2. Linear fit for URC shape coefficients*

	α	β
c_0	-1.56 ± 0.24	-2.14 ± 0.17
c_1	-0.076 ± 0.011	-0.117 ± 0.008

* $\alpha = \max(c_{\alpha 0} + c_{\alpha 1}\, mag, 0)$, $\beta = c_{\beta 0} + c_{\beta 1}\, mag$, $\gamma = 1 - \alpha - \beta$

On the other hand, our dark mass density distribution is different from the spherically symmetric cored one. The luminous matter is located in a plane $\rho_{lm} \sim \delta(z)$, while the dark matter is coupled to it by KT-integral. This integral is not spherically symmetric and, as the detailed analysis shows, contains a similar z-singularity. Nevertheless, the corresponding dark mass contribution to the in-plane squared velocity near the center is *the same* as for the cored distribution.

The other difference from [8] is the central term $v^2_{center,dm} = Const$ activated at higher luminosity bins. It corresponds to the non-cored distribution with the original unbounded $\rho_{center,dm} \sim r^{-2}$ dependence. This dependence is valid as long as the center remains unresolved, while for the distances in the bulge region, it starts to show the cored behavior. Only the dark matter contribution of supermassive black hole in the center of the galaxy remains unresolved till its gravitational radius, however, it does not prevail over the other central structures in the model. In the next section we will follow the distance scale into the bulge and consider this question in more detail.

3. RDM-stars and GRC

In the paper by Sofue [14] the experimental rotation curve for the entire Milky Way galaxy has been presented. This curve, continuously covering the range of distances from the Galactic Center to the size of the Local Group, is shown on Fig.4. In linear scale on the left there is a large segment of the curve in the range 3-15kpc that looks approximately flat. In logarithmic scale on the right one can see more complicated structures: the minimum of the curve beyond 100kpc, where the dark halo ends, two maxima near 0.5kpc and 0.01kpc, corresponding to the main bulge and the inner bulge, in terminology of [14], and the central 1pc zone of Keplerian domination of the supermassive black hole, shown by the dashed line.

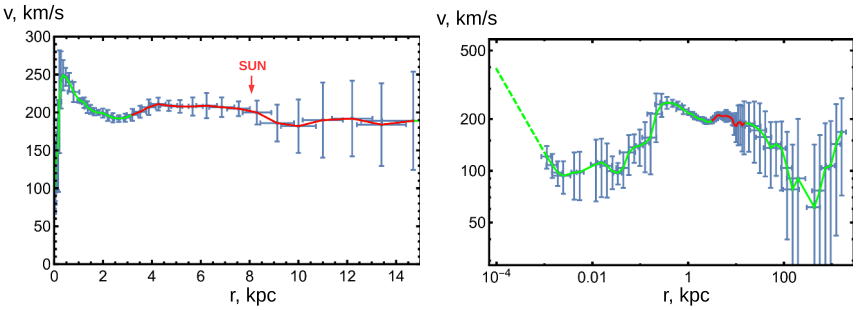

Figure 4. GRC in linear and logarithmic scale. Data from [14].

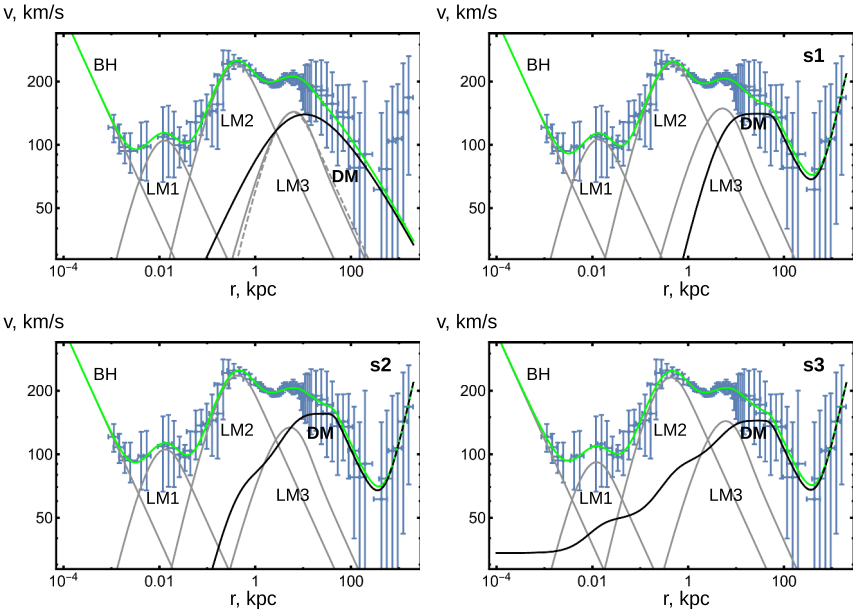

Figure 5. Model fits of the GRC. Top left – the fit [14] with NFW DM profile; other plots – RDM model fits for three coupling scenarios. BH is the Keplerian contribution of the central black hole; LM1-3 are contributions of luminous matter from the inner bulge, the main bulge and the disk; DM is the dark matter contribution. The green line is the quadratic sum of these contributions.

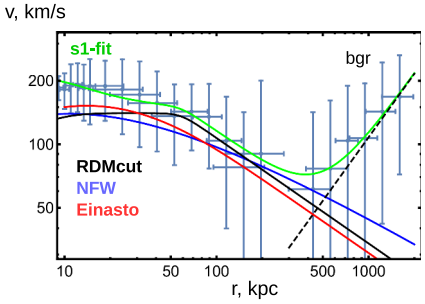

Figure 6. The outer part of the GRC with different dark matter profiles.

Table 3. GRC: fixed DM coupling coefficients for 3 scenarios

λ_{KT}	s1	s2	s3
λ_{smbh}	0	1	10^3
λ_1	0	1	10^2
λ_2	0	1	2
λ_{disk}	1	1	1

Table 4. GRC: fitting results, log of parameters and their errors*

$\log(par)$	s1	s2	s3
M_{smbh}	15.1 ± 0.2	15.1 ± 0.2	15.0 ± 0.3
M_1	17.8 ± 0.3	17.8 ± 0.3	17.4 ± 0.5
a_1	-5.5 ± 0.4	-5.5 ± 0.4	-5.6 ± 0.4
M_2	22.99 ± 0.04	22.88 ± 0.13	22.83 ± 0.13
a_2	-1.99 ± 0.07	-2.05 ± 0.10	-2.05 ± 0.09
M_{disk}	24.2 ± 0.8	24.0 ± 0.8	24.3 ± 0.5
R_D	0.9 ± 0.3	0.91 ± 0.17	1.04 ± 0.11
L_{KT}	1.9 ± 1.4	1.8 ± 1.1	2.5 ± 0.8
R_{cut}	4.1 ± 0.9	3.8 ± 0.7	4.0 ± 0.7
ρ_0	6.5 ± 0.8	6.5 ± 0.7	6.5 ± 0.8

* masses in $M_\odot$, lengths in kpc, density in $M_\odot/kpc^3$

Table 5. GRC: fitting results, central values of parameters*

par	s1	s2	s3
M_{smbh}	3.6×10^6	3.6×10^6	3.2×10^6
M_1	5.5×10^7	5.2×10^7	3.6×10^7
a_1	0.0041	0.0039	0.0036
M_2	9.7×10^9	8.6×10^9	8.2×10^9
a_2	0.13	0.13	0.13
M_{disk}	3.2×10^{10}	2.7×10^{10}	3.5×10^{10}
R_D	2.4	2.5	2.8
L_{KT}	7.0	6.3	12.0
R_{cut}	58	45	53
ρ_0	646	653	649
ϵ_{smbh}	0	$3.1 \cdot 10^{-11}$	$1.6 \cdot 10^{-8}$
$M_{dm}(R_{cut})$	2.7×10^{11}	2.5×10^{11}	2.6×10^{11}
$R_{opt} = 3.2R_D$	7.7	8.0	9.0
$x = L_{KT}/R_{cut}$	0.12	0.14	0.23

* masses in $M_\odot$, lengths in kpc, density in $M_\odot/kpc^3$

GRC uses the *exponential spheroid model* [14] for the bulges, describing the volumetric mass density by an exponent $\rho_{lm} \sim \exp(-r/a)$. In Appendix A we evaluate the KT-integral for such a distribution. Unifying it with the luminous matter contributions from [14], we obtain the following model:

$$v^2_{smbh} = G_m M_{smbh}/r,\ G_m = 4.3016 \cdot 10^{-6}\ (km/s)^2(kpc/M_\odot), \tag{13}$$
$$v^2_{sph,i} = G_m M_i/r \cdot F_{sph}(r/a_i),\ i = 1, 2,\ v^2_{disk} = G_m M_{disk}/(2R_D) \cdot F_{disk}(r/R_D), \tag{14}$$
$$F_{sph}(x) = 1 - e^{-x}(1 + x + x^2/2),\ F_{disk}(x) = x^2(I_0(x/2)K_0(x/2) - I_1(x/2)K_1(x/2)), \tag{15}$$
$$v^2_{lm} = v^2_{smbh} + v^2_{sph1} + v^2_{sph2} + v^2_{disk}, \tag{16}$$
$$v^2_{dm,bh} = G_m M_{smbh}\lambda_{smbh}/L_{KT},\ v^2_{dm,sph,i} = G_m M_i \lambda_{sph,i}/L_{KT} \cdot F_{dm,sph}(r/a_i), \tag{17}$$
$$F_{dm,sph}(x) = (6x + (3 - 3x + x^2)e^x Ei(-x) - (3 + 3x + x^2)e^{-x}Ei(x))/(4x), \tag{18}$$
$$v^2_{dm,disk} = G_m M_{disk}\lambda_{disk}/L_{KT} \cdot F_{dm,disk}(r/R_D),\ F_{dm,disk}(x) = 1 - e^{-x}(1 + x), \tag{19}$$
$$v^2_{dm,sum} = v^2_{dm,bh} + v^2_{dm,sph1} + v^2_{dm,sph2} + v^2_{dm,disk},\ v^2_{bgr} = 4\pi G_m \rho_0 r^2/3, \tag{20}$$
$$v^2_{dm,cut} = v^2_{dm,sum}(r \to R_{cut}) \cdot R_{cut}/r,\ v^2_{dm} = ((v^2_{dm,sum})^p + (v^2_{dm,cut})^p)^{1/p}, \tag{21}$$
$$v^2 = v^2_{lm} + v^2_{dm} + v^2_{bgr}. \tag{22}$$

Here I_n, K_n are the modified Bessel functions, Ei is the exponential integral function. G_m represents the gravitational constant G in the model system of units, measuring masses in $M_\odot$, lengths in kpc, velocities in km/s.

The features of the rotation curve at large distances are simulated as follows. We perform a cut of dark matter density on the outer distance R_{cut}, to obtain a halo of a finite radius. At larger distances the rotation curve switches to the Keplerian regime $v^2_{dm,cut}(r)$. A similar cut has been also performed in [23]. Then, to join the increasing function $v^2_{dm,sum}(r)$ and the decreasing function $v^2_{dm,cut}(r)$ we take $v^2_{dm} = \min(v^2_{dm,sum}, v^2_{dm,cut})$, define it as $L_{-\infty}$-norm, then replace it by a smooth L_p-norm with a numerical value $p = -10$. These manipulations on the rotation curve have negligible influence on the fitting procedure, it is only important that a flat dark matter profile is changed to the falling profile at large distances. We also add a uniform background mass density contribution v^2_{bgr} to simulate the increase of the rotation curve after the minimum.

We introduce the dimensionless coefficients λ_i, defining the coupling of dark matter to different components of the luminous matter. This allows to take into account a different concentration or a different population of black holes in different components. The resulting dark matter contributions (smbh,sph,disk) have a common form, $G_m M_i \lambda_i / L_{KT}$ multiplied to a function of r, tending to unity when $r \to \infty$. If the cutting is performed at sufficiently large R_{cut}, the total enclosed mass of dark matter is

$$M_{dm}(R_{cut}) = v^2_{dm,sum}(R_{cut})R_{cut}/G_m = R_{cut}/L_{KT} \cdot \tag{23}$$
$$(\lambda_{smbh}M_{smbh} + \lambda_{sph1}M_1 + \lambda_{sph2}M_2 + \lambda_{disk}M_{disk}). \tag{24}$$

The results of the fit are presented in Fig.5. The top left image shows the fit of [14], where the NFW profile has been taken to represent the dark matter halo. The BH part corresponds to the Keplerian contribution of the central black hole; LM1 and LM2 are the luminous mass spheroidal contributions of the inner and the main bulge. The LM3 solid line corresponds to the luminous mass disk contribution, while the dashed line shows a spheroidal contribution close to it. These two contributions look similar, but differ in details. In particular, they possess slightly different asymptotics at $r \to 0$, $v^2_{sph} \sim r^2$ vs $v^2_{disk} \sim r^2(-\log r)$. The last formula is obtained by decomposing the Bessel functions in (15). The velocity squared sum shown by the green line fits the experimental data perfectly.

The next three images in Fig.5 show the fit of the same data by the model constructed in this paper, for three different selections of λ_i coefficients shown in Table 3. As we see, they fit the experimental data perfectly as well. This means that the fit of the data can neither favor NFW/RDM profile nor decide between RDM scenarios with different couplings. A possible reason is that the rotation curve of the Milky Way seems to be dominated by the luminous matter, while the dark matter becomes important only at the large distances, where the data scatter is so large. As a result, quite different dark matter profiles can describe the same data equally good.

The resulting composition of the galaxy shows the strong hierarchy of masses and distances:

$$M_{smbh} \ll M_1 \ll M_2 \ll M_{disk} \ll M_{dm},\ a_1 \ll a_2 \ll R_D \ll R_{cut}. \tag{25}$$

The coupling length L_{KT} varies between the scenarios and is of the order of $R_{opt} = 3.2R_D$.

The baryon fraction $M_{lm}/(M_{lm} + M_{dm}(R_{cut}))$ for the data in Table 5 varies in the range 0.12-0.14. It is located between the estimation 0.12 for the groups of galaxies [13, 27] and the cosmological value 0.17 from WMAP [28], corrected later to 0.16 by Planck observations [29].

The background density $\rho_0 \sim 650 M_\odot/kpc^3$ is approximately 5 times greater than the critical density $\rho_{c0} = 3H_0^2/(8\pi G) \sim 126 M_\odot/kpc^3$, evaluated for $H_0 = 67.4\ km/s/Mpc$ [29]. This result indicates the background mass overdensity in the Local Group in comparison with the cosmological value.

In more detail, assuming that the background density is composed of the uniform baryonic, dark matter and dark energy contributions in the Local Group, we have: $\rho_0 = \rho_{bLG} + \rho_{dmLG} - 2\rho_\Lambda$. Here we took the effective negative contribution for dark energy term (see, e.g., Blau [30]). Thus, we have $\rho_0/\rho_{c0} = \Omega_{bLG} + \Omega_{dmLG} - 2\Omega_{\Lambda 0}$. Using the known $\Omega_{\Lambda 0} = 0.68$ [29] and the observed $\rho_0/\rho_{c0} \sim 5$, for the local overdensity of the baryonic and dark matter contribution relative to the cosmological value we obtain:

$$(\Omega_{bLG} + \Omega_{dmLG})/(\Omega_{b0} + \Omega_{dm0}) = (\rho_0/\rho_{c0} + 2\Omega_{\Lambda 0})/(1 - \Omega_{\Lambda 0}) \sim 20. \tag{26}$$

The outer part of the rotation curve. The modeling of the outer rotation curve in the dark matter halo uses Navarro-Frenk-White (NFW) profile [14] or Burkert profile [9], which has the same outer asymptotics as NFW one. The NFW profile originates from *numerical N-body simulations* of galaxies. Note that there are many other profiles used to describe the simulations. The paper by Merritt et al. [31] argues that the Einasto profile describes the simulations better than the NFW one.

On Fig.6 we display these two profiles together with the smoothed cutoff of RDM density used in our model. The profiles are given by the formulae

$$v_{NFW}^2 \sim F_{NFW}(r/r_x)/r,\ F_{NFW}(x) = \log(1+x) - x/(1+x), \tag{27}$$

$$v_E^2 \sim \gamma(3n, d_n(r/r_E)^{1/n})/r,\ d_n = 3n - 1/3 + 0.0079/n, \tag{28}$$

where $\gamma(n, x)$ is the lower incomplete gamma function. The parameters for Fig.6 are selected to $r_x = 5$; $n = 3$, $r_E = 21$. We see that the profiles closely follow each other in the corridor of the large data scatter.

Comparison with other solutions. One remark on the cutoff used in our model. We suppose that a transition from radial to uniform type of dark matter distribution happens on the outer radius of the galaxy. This phenomenon can be similar to *a termination shock* in the transitional layer on the border of the solar system, where the radially directed solar wind meets the uniform interstellar medium. In this paper we do not model this transition exactly, but simulate it by means of phenomenological cutoff.

Continuing the analogy with termination shock, we consider a transition happening at the outer radius of the galaxy, from *hot radial* dark matter inside to the *cold isotropic* type outside. In paper [32] a different scenario has been considered, assuming isotropic dark matter throughout the galaxy. A particular solution has been presented, where a halo of cold isotropic dark matter produces non-relativistic orbital velocities, while a similarly shaped halo of hot isotropic dark matter produces relativistic orbital velocities. The observed rotation curves are non-relativistic, this is commonly considered as an argument in favour of cold dark matter composing the galaxies.

On the other hand, it has been shown in [1] that the radial dark matter behaves differently. Technically, the difference is in the absence of transverse pressure components, that principally changes the equations and the structure of their solutions. For RDM solutions, the orbital velocities depend only on intensity factor, not on the type of matter. The radial dark matter can be massive, null or, theoretically, tachyonic (M/N/T-RDM), in all these cases the orbital velocities can be non-relativistic, at small intensity factors. In the RDM model, the rotation curves do not determine the type of dark matter. We select hot types, including N/T-RDM and high velocity MRDM configurations. In these cases the rays of dark matter are not strongly curved by the galactic gravitational field, so that RDM-stars appear, approximately, as spherically symmetric radially diverging dark matter distributions. Low velocity MRDM case is possible, in principle, but requires more complex computations, due to the bending of the dark matter rays.

4. RDM-stars and FRBs

In strong gravitational fields, an RDM-star Fig.1 is described by a system of non-linear differential equations. This system was solved numerically in [1], the main features of the solution are presented here in Appendix B. The first non-trivial result answers the principal question on how the black holes can emit something, dark matter in our case. The computation shows that the crossed matter flows erase the event horizon. For the decreasing radius r the enclosed mass $M(r)$ decreases (imagine how layers of positive mass are successively removed from the star). If the mass decreases sufficiently fast, so that the inequality $2GM(r)/c^2 < r$ holds everywhere, then the event horizon is not formed. The computation shows that this inequality holds for the RDM-star. Thus, RDM-stars are not black holes in the exact sense of the word, they are *quasi-black holes*, in terminology of [2]. These are the models where the solution closely follows the Schwarzschild profile till the gravitational radius and then behaves quite differently.

The typical solution of the RDM model in strong fields is shown on Fig. 7 left. The solution is computed for the parameters of the MW galaxy. It is defined by the metric coefficients $A > 0$, $B > 0$, where the first coefficient determines the effect of time dilation $dt_{in} = dt_{out}A^{1/2}$, and the second one – the effect of the curvature of the space $dL_{rad} = drB^{1/2}$. Here $dt_{in,out}$ is the time measured by an observer at rest, respectively, inside the object and outside, at a large distance from the object, while the value of the A-function at large distances is set to 1 by an agreement. The same function defines the redshift of the wavelength $\lambda_{out} = \lambda_{in}A^{-1/2}$ for the light coming out of the object, as well as the inverse effect of blueshift and, in general, an increase in the energy of any kind of matter falling on the object, $E_{in} = E_{out}A^{-1/2}$. Another metric coefficient determines the variation of the proper element of length in the radial direction dL_{rad} with respect to the variation of the radial coordinate dr. It also defines the enclosed mass function, the Misner-Sharp mass: $M = (1 - B^{-1})\, r/2 < r/2$, in geometric units ($G = c = 1$). The radial coordinate, also called *aerial radius*, defines an element of proper length in the tangential direction, by the variation of the angle $dL_{tan} = rd\theta$, as well as the area of r-sphere as $4\pi r^2$. Further details about the equations and metric coefficients can be found in the Appendix B.

Due to the strong variation of the metric coefficients on the RDM solution, it is given in logarithmic coordinates:

$$x = \log r,\ a = \log A,\ b = \log B. \tag{29}$$

Even taking the logarithm here is not enough, the resulting solution is difficult to depict on one graph. In Fig.7 left we show the part of the solution. The starting point of integration 1 corresponds to the edge of the MW galaxy and is located outside the graph, with $x_1 \sim 49.5$ (for r in meters). Further, the solution reaches a maximum of b at point 2, while the other coefficient falls approximately symmetrically as $a \sim -b$. This behavior corresponds to the Schwarzschild regime, for which the functions A, B are inverse to each other, $A = 1 - r_s/r$, $B = A^{-1}$, where r_s is the Schwarzschild radius. The values of B reached at point 2 are really large $B_2 \sim 6.25 \cdot 10^5$. Next comes *red supershift* mode, in which a, b fall almost parallel to each other, $b = a + Const$, with almost constant x. There are some further interesting structures 3 outside the graph, however, we will make a stop earlier.

The rapid fall of metric coefficients is accompanied by rapid increase of the mass density. This phenomenon was earlier considered in [15]. For crossed matter flows, the increase of their energy leads to the increase of pressure, that contributes to the increase of gravitational field and that produces the further increase of energy. This positive feedback loop leads to the rapid increase of energy, pressure and mass density, denoted in [15] as *mass inflation*. Practically, the mass density very rapidly reaches Planck values, after that our model should be modified.

Quantum Gravity (QG) computations applied for a cosmological model with a scalar field [33–35] show that the quantum corrections modify the mass density as follows:

$$\rho_{\text{eff}} = \rho\,(1 - \rho/\rho_c), \tag{30}$$

when the density exceeds the critical value of the order of Planck density $\rho > \rho_c \sim \rho_P$, the gravitational force becomes repulsive. Formally, the mass density becomes negative, although this result is often interpreted as a quantum pressure due to the Heisenberg principle. The model of *Planck stars* [16] is built on this result, proposing that in a collapse of stars, upon reaching the Planck density, *a quantum bounce* phenomenon happens, the collapsing matter is thrown back, the black hole becomes white.

We will consider a stationary version of this model, where the formed *Planck core* inside an RDM-star is stabilized by the pressure of dark matter flows. For this purpose on reaching the Planck density we perform a QG-cutoff in the model, in geometric units $\rho \sim l_P^{-2}$, where l_P is the Planck length. The QG-cutoff is shown by straight line on Fig.7 left.

For definiteness, we will consider null radial dark matter (NRDM), although the solution structure weakly depends on the type of matter. The density and radial pressure of matter is determined by the formula

$$\rho = p_r = \epsilon/(8\pi r^2 A). \tag{31}$$

At large distances, the gravitating density is determined by the sum $\rho_{grav} = \rho + p_r$. This is the density participating in (3) and the other formulas of the previous sections. The parameter ϵ is related with the asymptotic orbital velocity at large distances as $\epsilon = (v_a/c)^2$. For MW the choice $v_a = 200$km/s gives $\epsilon = 4 \cdot 10^{-7}$.

The condition $\rho \sim l_P^{-2}$ is reached in the region of a rapid drop of the coefficients a, b that occurs at almost constant $r \sim r_s$. The intersection with QG-line is located at

$$A_{QG} = \epsilon\,(l_P/r_s)^2/(8\pi). \tag{32}$$

The numerical values of this coefficient for the parameters of MW galaxy correspond to the redshift factor $A_{QG}^{1/2} = 1.7 \cdot 10^{-49}$. This is also a key formula that determines the redshift factor for the photons emitted from the surface of the Planck core, as well as an increase in the kinetic energy of the matter falling from the outside onto the Planck core. How the Planck core is composed is unknown. We will simply assume that the core is filled with a fluid or a

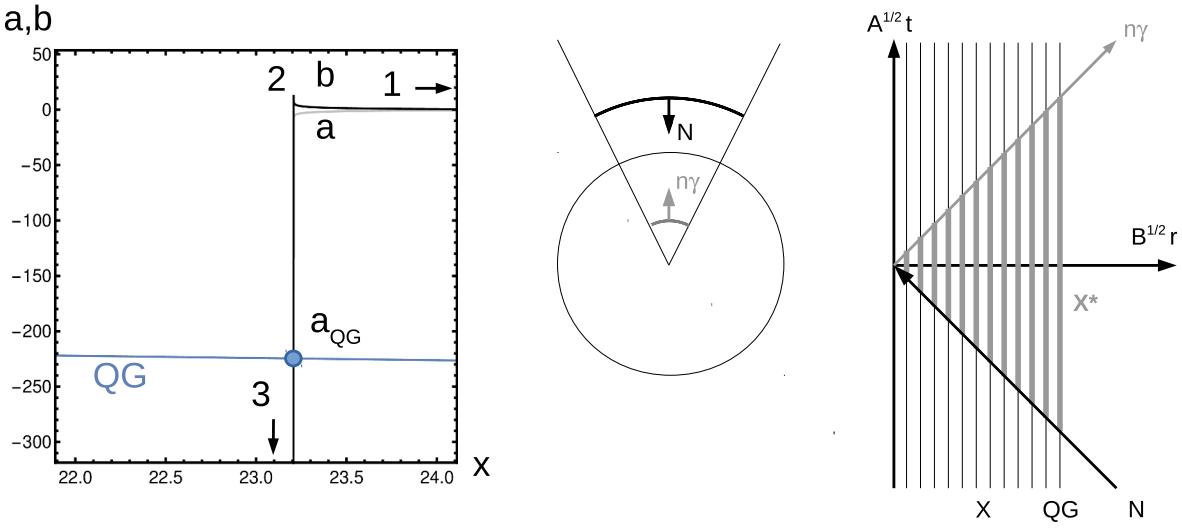

Figure 7. On the left: behavior of metric coefficients, for an RDM-star with parameters of the Milky Way galaxy. The QG-line shows the quantum gravity cutoff. In the center: a mechanism of coherent FRB emission in the RDM model. An asteroid transformed to a Lorentz-contracted ultrarelativistic thin shell (N) falls onto the Planck core and produces a shockwave, energizing the medium in the core. Then the shockwave bounces from the center and stimulates an emission of photons ($n\gamma$) from the energized medium. On the right: temporal diagram of the process.

gas consisting of particles of a mass of the order of Planck one. The estimation in Appendix B shows that under the influence of the external pressure of dark matter, the Planck core must have a slight overdensity over the critical value $\Delta\rho/\rho_P \sim 3\epsilon$, so that the resulting repulsive force balances this pressure.

The considered system is able to generate FRBs via the following mechanism. The characteristic total burst energy [36] reaches $\sim 10^{32\text{-}34}$ J, or $\sim 10^{15\text{-}17}$ kg in mass equivalent, which is the mass of an asteroid. First, we assume an energy conversion efficiency of the order of unity and consider an external object of the order of the mass of an asteroid falling on an RDM-star. As a result of the action of tidal forces and superstrong acceleration, the object will be split into component particles, for which we will consider nucleons, that is, protons or neutrons. In fact, the splitting can go further, to quarks, or stop earlier, at the level of nuclei. The RDM-star acts as a superstrong particle accelerator, boosting the particles falling on it to ultrarelativistic velocities corresponding to the particles energy $E_N \sim m_N A_{QG}^{-1/2}$, where m_N is their rest mass. These accelerated particles fall onto the Planck core and are scattered on it as on a fixed target. Accelerated particles of energy E_N enter into reactions with the particles of mass m_X composing the core. In the reactions, high-energy photons are released that go outside with the redshift factor $A_{QG}^{1/2}$. These photons represent an FRB.

Further estimations depend on the type of reactions occurring inside the Planck core. First, we assume that as a result of the reactions, photons are born with the energy of the order of the energy of the accelerated particles $E_{\gamma,in} \sim E_N$, as it occurs, for example, for *Bremsstrahlung* near the cutoff frequency. Since the acceleration and the redshift factors cancel each other, the outgoing photons have energy $E_{\gamma,out} \sim m_N$ in the region of 1 GeV, the wavelength is of the order of the Compton length for the nucleon $\sim 10^{-15}$ m, gamma radiation. Interestingly, this answer is close to the estimate $\sim 10^{-16}$ m [16] for Planck stars, obtained from completely different considerations.

Since the typical FRB wavelengths differ by 14 orders of magnitude from this value, it is necessary to look for another mechanism. Suppose that inelastic scattering of incoming particles on X-particles occurs, in which an excited state X_1^* is born with the energy $E(X_1^*) \sim \sqrt{2m_X E_N}$. This is the maximum amount of energy that can be released in the inelastic collision of m_N and m_X in their center of mass system, which follows from the kinematics of the process at $E_N \gg m_X \gg m_N$. After this collision, the excited particle and the nucleon move with the same speeds, and due to $E(X_1^*) \ll E_N$, their energy is almost equal to the original $\sim E_N$. Further, these particles enter into the inelastic collision with the next X-particle, which also goes into the excited state, X_2^*. This *snowball effect* continues until all the kinetic energy of the initial particle is spent. Thus, a column of excited particles will be born, each of energy $E(X_n^*) \sim E(X_1^*)n^{-1/2}/2$, which will be confirmed by the calculation in Appendix C. The specific form of this spectrum is currently not so important, note that the energy of the first excited state $E(X_1^*)$ scales the entire spectrum and cuts it from above. At the end of this process, all particles will be stopped, and all the initial kinetic energy will be deposited into the energy of the excited states X_n^*.

Then the particles transfer from the excited state to the initial state with the emission of one photon: $X_n^* \to X + \gamma$. Due to the fact that $E(X_n^*) \gg m_X$, the photon receives only a half of the excitation energy of the particle, $E_{\gamma,in} \sim E(X_n^*)/2$. The other half goes into recoil of the particle X, and, ultimately, into the thermal energy. Already here we see that only a part of the initial kinetic energy of the asteroid can be transformed into FRB energy, and the energy relations will require corrections, which we will consider below.

The observed energies of the produced photons, at the maximum frequency, after taking into account the redshift are $E_{\gamma,out} = E(X_1^*)/2 \cdot A_{QG}^{1/2}$, which, after substitutions, gives the wavelength

$$\lambda_{out} = \sqrt{2\lambda_X \lambda_N}\, A_{QG}^{-1/4}, \tag{33}$$

where λ_X and λ_N are Compton wavelengths of particles X and N respectively. Assuming $\lambda_X = l_P$, which corresponds to the mass $m_X = 2\pi m_P$, and substituting (32), obtain

$$\lambda_{out} = 2(2\pi)^{1/4} \sqrt{r_s \lambda_N}\, /\epsilon^{1/4}. \tag{34}$$

Substituting here the Compton length of the nucleon and galactic parameters [37, 38]:

$$\lambda_N = 1.32 \cdot 10^{-15}\text{m},\ r_s = 1.2 \cdot 10^{10}\text{m},\ \epsilon = 4 \cdot 10^{-7}, \tag{35}$$

obtain

$$\lambda_{out} = 0.5\text{m},\ \nu_{out} = 0.6\text{GHz}, \tag{36}$$

that falls in 0.111 ... 8GHz, the characteristic range of FRB observations (exactly to the central frequency of CHIME/FRB180725A observation).

In fact, due to many side effects, it is not currently possible to make an accurate calculation of the observed FRB characteristics. These signals are broadband, a single observation usually covers a range of the frequencies. The repeating signal FRB 121102 was recorded on 111MHz [39], it was also active around 1GHz [40, 41], and its maximum observed frequency is 8GHz [42–44]. This suggests that the frequency of this FRB source may float or have components in a wide band. The observed wavelength is also subject to a cosmological redshift, in the range of $z = 0.2$-1.5 [36]. At the same time, the value of z is not precisely measured, but inferred with a number of additional assumptions, discussed in more detail below. If we treat this correction as a measurement uncertainty, the frequency emitted on the host can be up to $1 + z \sim 2.5$ times higher than the observed one.

Also, our simple model will only make an estimate in order of magnitude. This estimate represents the upper bound for the observed FRB frequencies corresponding to the maximum possible energy of the emitted photons in the considered type of reactions. This estimate is valid only in order of magnitude, since the requirement that the solution reaches Planck density really does not give a sharp switch of QG-effects, but only an approximate position. One can introduce an attenuation factor, which marks the switch of QG-effects with a margin, when the density is $\rho = l_P^{-2}/s_1$. The final result depends mildly on this factor and we will allow a guess $s_1 = 1...10$ for its value. Also, we noted that the original particles can be not nucleons, but quarks or nuclei, which gives another factor $\lambda_N \to \lambda_N/s_2$, varying between 1/3 for the constituent quarks and ~ 56 for iron nuclei. With these corrections we get

$$A = s_1\epsilon\,(l_P/r_s)^2/(8\pi),\ \lambda_{out} = s_1^{-1/4}s_2^{-1/2}2(2\pi)^{1/4}\sqrt{r_s\lambda_N}\,/\epsilon^{1/4}, \tag{37}$$

$$\lambda_{out} = 0.038...0.87\text{m},\ \nu_{out} = 0.35...8\text{GHz}, \tag{38}$$

which gives a good overlap of the observed frequency band by our prediction.

The frequency range of the FRB is not the only, but the most stably predictable feature. Let's discuss briefly the possibility of reconstructing other parameters.

Energy spectrum of the burst. The computation in Appendix C shows, that in the spectral region immediately adjacent to the threshold, the energies of the excited states are $E(X_1^*) = (2m_X E_N)^{1/2}$, $E(X_n^*) \sim E(X_1^*)n^{-1/2}/2$. The number of photons in a given frequency interval is proportional to $|dn/dE|$, while the energy density is proportional to $E|dn/dE| = |d\log E/dn|^{-1} \sim 2n \sim (2E/E(X_1^*))^{-2}$, which implies the initial energy of the process with the spectral index $\alpha = -2$, $E|dn/dE| \sim E^\alpha$. The redshift scales the common factor $E(X_1^*)$ and does not change the density $E|dn/dE|$ and its spectral index. Note also that the spectral index is usually measured for flux density, and is also divided by the duration of the burst in a given frequency band. The process considered here corresponds to the initial flux density with a spectral index of -2, assuming that the intrinsic burst duration is constant in frequency.

The spectral index calculated here corresponds to a specific mechanism, the snowball effect, used to generate the excited states. This index may change when considering other mechanisms, such as particle showers, collision cascades, the scattering of high-energy nucleons on gas of Planck particles, as well as the scattering of the produced photons, both on the Planck gas and on the surrounding dark star environment. Experimental measurements give a spectral index that varies widely, $-10.4...13.6$, according to FRBCAT. This may mean high variability of this parameter between different bursts, as well as the inaccuracy of its experimental determination. The cutoff frequency is a more stable parameter, since it is determined by the maximum energy that can be deposited and then radiated as photons, and it is characteristic for the scattering of high-energy particles on a fixed target.

Total energy of the burst is determined by the mass of the object falling on the RDM-star. According to the mechanism discussed above, half of the rest energy of an object is converted into photons, with associated recoil efficiency $\eta_{rec} = 0.5$. At the same time, the energy spectrum for the considered process is strongly skewed to the left. In Appendix C we estimate the energy located in the frequency range $[\nu_{out}/10, \nu_{out}]$ as a small fraction of the total available energy, corresponding to the spectral efficiency of $\eta_{spec} \sim 5 \cdot 10^{-14}$. To compensate for this factor, the mass of the falling object must be $2 \cdot 10^{13}$ times larger, i.e., $\sim 2 \cdot 10^{28\text{-}30}$ kg, from 0.01 to 1 solar mass.

On the other hand, the reported experimental estimates for the total energy use the assumption that the burst is isotropic, which may also require corrections if the radiation has the form of a narrow beam. In this case, the total burst energy and the required mass of the external object can be significantly less than the isotropic estimate. Considering an object of diameter D on the surface of a sphere of radius $r_s \gg D$, the angular size of the beam can be

D/r_s. As we showed in Appendix B, a peculiar phenomenon of *gravitational beaming* occurs in the depth of the RDM-star, as a result of which the emission of photons in strictly radial direction becomes preferable, this supports the beam geometry considered here. On the other hand, after leaving the RDM-star, the wavelength of photons increases and the beam broadening starts to dominate according to the wave optics law λ/D. The efficiency of the beam energy transfer compared to isotropic one is $\eta_{beam} \sim 10^{8\text{-}12}$, for $D = 10$ km and the considered frequency range. This compensates a significant part of the estimated spectral losses. Thus, a falling object can still be a mass of the order of an asteroid, if the energy leakage in the low-frequency region is compensated by the radiation in the form of a narrow beam.

Coherence of the radiation is usually explained by superradiance [45] or stimulated emission [46]. We consider here the more general mechanism, stimulated emission, which is the basis of the work of lasers or masers. This mechanism is illustrated in Fig.7, the central image. At the top left, an asteroid is shown, transformed to a thin ultrarelativistic shell by Lorentz contraction. Due to gravitational beaming, radial trajectories are preferred for both incoming nucleons N and outgoing photons γ. Upon striking the surface of the Planck core, the shell excites a shockwave inside the conical area of the core marked in the figure. The Planck particles in this zone are excited $X \to X^*$, as a result of the simple snowball effect that we used for the estimates, or another mechanism that has the same inelastic scattering threshold E_N on m_X. The shockwave propagates close to the speed of light and reaches the center. Next comes the bounce of the shockwave. The mechanism of this bounce is the same as that of Planck stars, the compression of matter above the Planck density leads to the effect of gravitational repulsion. Further, the diverging shockwave initiates the reverse transitions $X^* \to X + \gamma$, stimulating the emission of photons in the conical region and causing them to coherently release all the stored energy.

The figure on the right shows the temporal diagram of this process. For definiteness, we consider the metric coefficients frozen, constant inside the Planck core. The incoming shell (N) and the shockwave it initiates $X \to X^*$ transitions, the excited states formed are shown in the figure by vertical thick gray lines. Further, the bounced shockwave causes the reverse transitions $X^* \to X + \gamma$, the resulting photons multiply each other ($n\gamma$) and move synchronously with the outgoing shockwave.

Temporal characteristics of the burst. For processes based on stimulated emission, one spontaneously emitted photon in its path causes the emission of subsequent photons synchronous with it, which can give very short durations. Under laboratory conditions, ultrashort pulses with a time bandwidth product (TBP) of the order of unity are achieved, that is, the minimum allowed by the uncertainty principle [47]. For FRB, this factor is much greater, for example, for [42] high-frequency FRB121102 repetition, component 11H, duration about 0.3 ms, bandwidth about 1 GHz, which corresponds to TBP $\sim 3 \cdot 10^5$. Thus, the pulse is obviously not as short as can be obtained in laboratory conditions, the duration of the pulse does not correspond to the width of the spectrum and has a different mechanism.

In the works [45, 48–55] it was noted that the frequency dependence of the pulse width is $W \sim \nu^\beta$, $\beta = -4... - 4.4$, which indicates the *scatter broadening* phenomenon when the signal propagates through the interstellar medium. The FRBCAT directory gives the scatter indices for 5 signals, all compatible with these values. The strongest scatter broadening manifests itself for 111 MHz low-frequency signals [39], for which the pulse width reaches several seconds instead of milliseconds at higher frequencies, which also agrees with an index of about -4. At high frequencies around 8 GHz, the effect of the interstellar scatter broadening is not as strong, and the observed durations in fractions of milliseconds can be an intrinsic signal characteristic or imparted by the local environment of the FRB source, see [42]. In the works [45, 49] it was also noted that for some signals broadening cannot be caused by the interstellar medium and most likely caused by a dense plasma near the FRB source. Both mechanisms are external and also can work for our model, scatter broadening in the interstellar medium and/or dense plasma

surrounding the RDM-star.

Repeating bursts. Till 2019 only one repeating signal FRB121102 was registered. Since that time a lot more repeating FRB signals have been detected, most on the new CHIME radio telescope. The cause of repeating bursts may be the passage of a massive object through the asteroid field, which was already proposed in [56]. If several asteroids fall on an RDM-star, with a time interval dt, then the interval between individual FRB flashes will also be dt. This follows from the stationarity of the solution, independently on the gravitational time dilation inside the RDM-star, the radial geodesics have the same shape and are shifted in time by dt according to the clock of the remote observer.

Dispersion measure (DM) characterizes the time delay of the signal, depending on the frequency as $dt_\nu \sim \nu^\gamma$. This delay is usually attributed to different propagation speeds of the electromagnetic signal in the interstellar medium, while the index with a high degree of accuracy is $\gamma = -2$. This delay determines the distance to the source and the cosmological redshift factor z, from which the total isotropic energy is extrapolated. However, as [45, 49] note, if scatter broadening occurs on the surrounding source environment, then a significant portion of DM can be also attributed to it.

Polarization. FRBs often exhibit a large degree of linear or circular polarization, see FRBCAT, as well as [57, 58] and references therein. This indicates the presence of strong magnetic fields near the source. To describe the polarization of the radiation of RDM-stars, a more sophisticated model will be needed, accounting for the magnetic field and also for the influence of strongly curved space-time in their interior.

Variability of different parameters between different bursts. We made calculations for the parameters of the central black hole in the MW galaxy, while the radiation can come from (quasi) black holes of other sizes. From (34) it can be seen that the observed wavelength of the FRB is preserved under scaling $r_s \to r_s s$, $\epsilon \to \epsilon s^2$. The values of A_{QG} are also preserved, as well as the values of the energy of incoming particles E_N and spectral efficiency η_{spec}. Thus, the mentioned FRB characteristics will be the same under constraint $\epsilon \sim r_s^2$.

This constraint can appear in frames of the following scenario. Assume that the energies E_0 of dark matter particles on the surface of Planck core are the same for different RDM-stars, e.g., are all of the order of Planck energy. Assume that the energies E_1 of these particles at the outer border of the galaxy are also the same, determined by the temperature of dark matter in the intergalactic space. In this case the redshift factor (32) will be also the same and (ϵ, r_s) values will be constrained as above.

Not all FRB characteristics are invariant under the considered scaling. E.g., η_{beam} depends on $\theta \sim \max(D/r_s, \lambda/D)$ and for small r_s must be re-estimated. Stellar black holes can generate FRBs with $\eta_{beam} \sim 1$. The fact that all FRBs are registered outside our galaxy can have a simple statistical explanation [59]. If a single FRB event has a small probability, evenly distributed over stellar black holes in billions of galaxies, then a hundred of recorded flashes will most likely occur outside our galaxy.

5. Combined analysis of RCs and FRBs in the RDM model

Let us obtain the constraints on the RDM model from the both types of measurements. At first, we separate contributions of the central supermassive and the stellar black holes. When analyzing the GRC, three scenarios were used, distinguished by the coupling coefficients of dark matter with individual galactic structures: the central black hole, the inner bulge, the outer bulge and the disk. The contribution to the intensity parameter for the central black hole is given by the formula

$$\epsilon_{smbh} = GM_{smbh}\lambda_{smbh}/(c^2 L_{KT}), \tag{39}$$

the resulting values of the parameter ϵ_{smbh} are given in Table 5. The absolute maximum of the parameter $\epsilon_{smbh} = 1.1 \cdot 10^{-7}$ corresponds to the absolute minimum speed $v_{min} = 100$km/s on

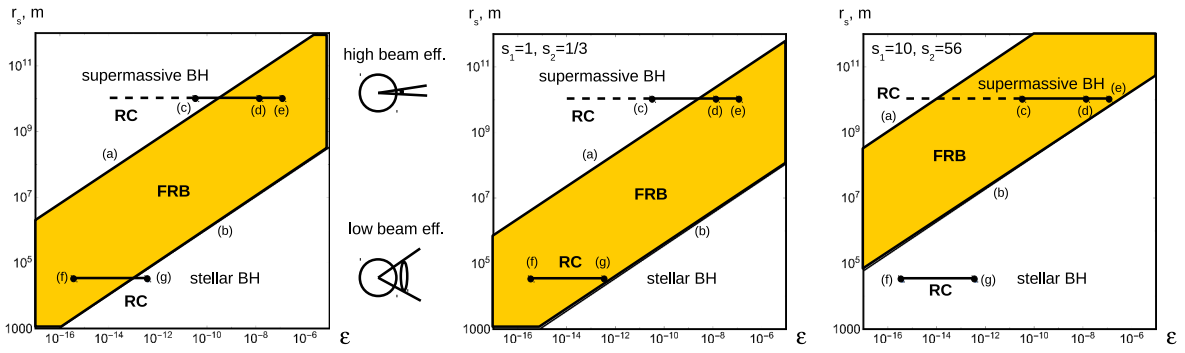

Figure 8. Combined analysis of RCs and FRBs. On the left: $s_{1,2} = 1$, in the center and on the right: with the variation of FRB tuning parameters $s_{1,2}$.

GRC in the bulge region, see Fig.4.

For stellar black holes of mass $M_{sbh} \sim 10M_{\odot}$, an equally distributed contribution to the ϵ parameter was assumed, that is, the total contribution is determined by the number of black holes, without taking into account their individual characteristics. For the total number of stellar black holes in our galaxy there is a broad estimate of $N_{sbh} = 10^6 - 10^9$, see [60] and references therein. Thus, we can estimate the contribution of each black hole from this class as $\epsilon_{sbh} = (\epsilon - \epsilon_{smbh})/N_{sbh}$, for $\epsilon = 4 \cdot 10^{-7}$.

In Fig.8, the results of the analysis of FRBs and RCs are combined. The band corresponds to the experimentally observed range of FRBs according to formula (34), (a) $\nu_{out} = 111$ MHz, (b) $\nu_{out} = 8$ GHz. The horizontal lines show the estimates obtained in the analysis of GRC: for the central supermassive black hole: (c) scenario s2, (d) scenario s3, (e) absolute maximum ϵ_{smbh} for MW; for the stellar black holes: (f) the estimate for $N_{sbh} = 10^9$, (g) the same for $N_{sbh} = 10^6$, assuming $\epsilon_{smbh} \ll \epsilon$.

First of all, we see that the intersection of the experimental characteristics under consideration exists, which means that the model is capable of describing both RC and FRB observations. There are two classes of solutions, the sources of FRBs can be both central supermassive and stellar black holes. Supermassive sources can be considered as more preferable. Since they have much larger radius, they have a smaller beam width and greater η_{beam} efficiency, which makes their registration more preferable. Also, dense plasma surrounding supermassive black holes can create a large scatter broadening, characteristic for the observed signals. In works [49, 52], the nuclei of other galaxies were also considered as the preferred sources of FRBs.

Using the formula (37) with tuning parameters, the band on the graphs is shifted, Fig.8 center for the minimum, right for the maximum values of FRB tuning parameters. After this variation, the intersection of the FRBs and RCs covers almost the entire band of observed frequencies. In particular, for the preferred scenario of supermassive black holes, only a narrow zone $\nu_{out} = 6.33...8$GHz remains uncovered, and this gap will close if r_s is a factor of 1.6 smaller or ϵ_{smbh} is a factor of 2.6 larger. Such variations of parameters can be attributed to the natural variability of the source.

To some extent, our analysis was related to the MW parameters extracted from its rotation curve. Thus, we characterize a subset of FRBs, whose sources are located in galaxies similar to MW by their parameters. It would be interesting to populate this diagram with data from other galaxies. For this, however, it is necessary that the galactic RC be resolved till the central black hole. This is required for the detailed fit or at least v_{min} estimate to find the contribution of the central black hole to the ϵ parameter. With insufficient resolution, the contributions of smbh

and bulge1,2 are accumulated in one term. As a result, all black holes contained in the central region (supermassive, intermediate mass, stellar) effectively gather into one large black hole. In our model, however, FRB occurs on distinct black holes, which requires an assessment of their individual parameters.

6. Conclusion

We have studied the detailed behavior of galactic rotation curves in the model of the RDM-stars. First of all, we considered the dark matter contribution to the gravitational field, calculated using KT-integral for a single RDM-star. The resulting gravitational field gives a flat rotation curve. Further, taking the distribution of RDM-stars in the galaxy proportional to the distribution of luminous matter, non-flat curves are obtained. These curves provide a good fit of the observational data, both for the URC describing general spiral galaxies and for the GRC describing the Milky Way in a wide range of distances.

Further, we have considered RDM-stars as possible sources of FRBs. The QG-cutoff creates a core of Planck density, filled with a gas of Planck mass particles, inside the RDM-star. FRBs are generated via the following mechanism. An asteroid falls onto an RDM-star. Large gravitational forces available in the interior accelerate the asteroid to extremely high energies, transforming it to a Lorentz-contracted thin ultrarelativistic shell. The shell falls onto the core and produces a radially converging shockwave, energizing the medium in a conic region of the core. The same shockwave after a bounce from the center, initiates a stimulated emission of energetic photons, releasing the energy, deposited to the medium, in a form of a short pulse of a coherent electromagnetic radiation. Further, strong redshift factor of RDM-star downscales the frequency of this radiation, leading to an observable FRB.

The estimation of an upper frequency, based on the kinematics of deep inelastic reactions between the nucleons composing the asteroid and Planck particles in the core, lead to a formula, involving only the nucleon mass, the gravitational radius and the flux of dark matter in the RDM-star. Substituting parameters of the central black hole in the Milky Way galaxy, we obtain the value 0.6GHz for this frequency. Introducing attenuation factors, regulating the QG-switch and particle granularity for the asteroid, we obtain the range 0.35-8GHz for the characteristic upper FRB frequency. This estimation fits well with the observable range 0.111-8GHz for the FRBs. We also discuss the reconstruction of other FRB parameters in frames of the model, including total energy, energy spectrum, shape of the beam and temporal characteristics of the pulse.

We have also performed a combined analysis of FRBs and RCs within the framework of the RDM model. We show that both the centers of spiral galaxies and the stellar black holes can be sources of FRBs, also after the model parameters are constrained by the observable RCs.

Acknowledgments

Many thanks to Paolo Salucci for his valuable remark on the behavior of experimental rotation curves, which has inspired the author for writing this paper. The author also thanks Kira Konich for proofreading the paper.

Appendix A. Fitting of rotation curves

Fitting of URC. Being applied to the galactic disk, the dark-to-luminous matter coupling (1-7) produces the following contribution to the orbital acceleration:

$$x = (r_1, 0),\ y = (r\cos\alpha, r\sin\alpha),\ a_{r,dm}(x) = G/L_{KT}\int dM_{lm}(y)\,(x-y)_1/(x-y)^2 \tag{A.1}$$

$$= G/L_{KT}\int r dr d\alpha\,\Sigma_{lm}(r)\,(x-y)_1/(x-y)^2 = G/L_{KT}\int_0^\infty r dr\,\Sigma_{lm}(r)\,\hat{I}_1(r_1, r), \tag{A.2}$$

$$\hat{I}_1(r_1, r) = \int_0^{2\pi} d\alpha\,(r_1 - r\cos\alpha)/(r^2 + r_1^2 - 2rr_1\cos\alpha) = 2\pi/r_1\cdot\theta(r_1 - r), \tag{A.3}$$

$$a_{r,dm}(r_1) = v^2_{dm}(r_1)/r_1 = G/(r_1 L_{KT}) \int_0^{r_1} 2\pi r dr\, \Sigma_{lm}(r) = GM_{lm}(r_1)/(r_1 L_{KT}), \tag{A.4}$$

$$\Sigma_{lm}(r) \sim \exp(-r/R_D),\ M_{lm}(r_1) = M_{lm} \cdot (1 - \exp(-r_1/R_D)(1 + r_1/R_D)). \tag{A.5}$$

It is necessary to make several comments at this point. It has been noted in [1], that the dark matter potential $\varphi_{dm} \sim \log r$ is *a fundamental solution* of Poisson equation in 2 dimensions. As a result, the dark matter in-plane gravitational acceleration is described by the enclosed mass function, in the same way as for spherically symmetric mass distribution in 3 dimensions. This property is confirmed by the straightforward computation above, where the internal integral $\hat{I}_1(r_1, r)$ over a circle is evaluated to the Heaviside θ-function, then the external integral in $a_{r,dm}(r_1)$ is cut at the upper limit r_1 and is represented by the luminous matter enclosed mass $M_{lm}(r_1)$. In these formulae $\Sigma_{lm}(r)$ is the luminous mass surface density, for which the exponential Freeman model [26] is taken. $M_{lm}(r_1)$ is the corresponding enclosed mass function and the common multiplier M_{lm} without the argument is the total disk mass.

The above described property of the dark matter potential allows to formulate the following set of simple rules for the enclosed mass:

- for spherically symmetric distribution of luminous matter, v^2_{lm} contribution is defined in terms of the enclosed luminous mass via Gauss theorem as $v^2_{lm} = GM_{lm}(r)/r$;
- for dark matter coupled to luminous matter via KT-integral and planar axially symmetric distribution of the luminous matter, in-plane v^2_{dm} contribution is defined in terms of the enclosed luminous mass as $v^2_{dm} = GM_{lm}(r)/L_{KT}$;
- asymptotically, for compact distribution of luminous matter at large distances, v^2_{lm} and v^2_{dm} contributions are defined in terms of the total enclosed luminous mass as $v^2_{lm} = GM_{lm}/r$ and $v^2_{dm} = GM_{lm}/L_{KT}$.

In the other cases, e.g., for exponential disk at moderate distances, the mass distribution is not spherically symmetric and v^2_{lm} contribution is not defined in terms of the enclosed mass by a local formula.

Note also that in paper [25] the dark-to-luminous matter coupling has been introduced in the form (1-2), then it has been modified by an oscillatory term. The main conclusions of [25] are preserved without this oscillatory term and we will also consider the version of KT-integral without the oscillatory term in this paper.

Now we will provide technical details about the used fitting procedure. The fitting parameters $(\alpha_0, \alpha, \beta, \gamma)$ enter linearly to the velocity squared formula. Mathematica `LinearModelFit` is used for fitting. At first, we fitted the experimental curves by all four basis forms including the contribution of central luminous matter with the coefficient α_0. As a result, we obtained the values α_0 comparable with zero. Further, we set $\alpha_0 = 0$ and repeated the fit with three basis forms. At the first four luminosity bins the obtained values for the coefficient α, regulating the contribution of central dark matter, was negative or comparable with zero up to an error. Also in the first luminosity bin the value β for the contribution of the luminous disk was comparable with zero. In those cases the values of the corresponding coefficients have been set to zero, and the fit was repeated with a reduced number of basis shapes. The obtained results are placed in Table 1.

The constraint $\alpha + \beta + \gamma = 1$ has not been imposed during the fit. However, since the experimental data have been normalized in the point $r/R_{opt} = 1$ to $v/v_{opt} = 1$ and the fitted curves follow this normalization closely, this constraint has been fulfilled up to an error on the fitting results. Then, in the range $-23.08 \le mag \le -18.29$, α and β coefficients have been linearly fitted with respect to mag, with the necessary clamp to avoid the negativity, see Fig.3 and Table 2, and the remaining coefficient γ has been found from normalization:

$$\alpha = \max(-1.56 - 0.076\, mag, 0),\ \beta = -2.14 - 0.117\, mag,\ \gamma = 1 - \alpha - \beta. \tag{A.6}$$

Fitting of GRC. Evaluation of KT-integrals for disk and bulge components is done by a straightforward computation:

$$x = (r_1, 0, 0),\ y = (r\cos\alpha, r\sin\alpha, 0),\ a_r(x) = G/L_{KT} \int dM_{lm}(y)\,(x-y)_1/(x-y)^2 \tag{A.7}$$

$$= G/L_{KT} \int r^2 dr\, 2\pi \sin\alpha\, d\alpha\, \rho_{lm}(r)\,(x-y)_1/(x-y)^2 = G/L_{KT} \int_0^\infty 2\pi r^2 dr \rho_{lm}(r)\, \hat{I}_2(r_1, r), \tag{A.8}$$

$$\hat{I}_2(r_1, r) = \int_0^\pi d\alpha\ \sin\alpha\,(r_1 - r\cos\alpha)/(r^2 + r_1^2 - 2rr_1\cos\alpha) = \int_{-1}^1 du\,(r_1 - ru)/(r^2 + r_1^2 - 2rr_1 u) \tag{A.9}$$

$$= (2rr_1 + (r^2 - r_1^2)\log(|r - r_1|/(r + r_1)))/(2rr_1^2),\ \rho_{lm}(r) = M_{lm}/(8\pi a^3) \cdot \exp(-r/a), \tag{A.10}$$

$$a_r(r_1) = GM_{lm}/(4a^3 L_{KT}) \int_0^\infty r^2 dr \exp(-r/a)\, \hat{I}_2(r_1, r) = GM_{lm}/(r_1 L_{KT}) \cdot \hat{I}_3(r_1/a), \tag{A.11}$$

$$\hat{I}_3(x) = ((3 - 3x + x^2)e^x Ei(-x) - (3 + 3x + x^2)e^{-x} Ei(x) + 6x)/(4x). \tag{A.12}$$

Now we provide the technical details on the fitting procedure. We perform the exponential substitution $par = \exp(lpar)$ and select the logarithms of all free variables as fitting parameters. Mathematica `NonlinearModelFit` is used for fitting. Table 4 presents the resulting values of these logarithms together with their standard errors. In Table 5 we present the central values of parameters in the physical units. The mass of the central black hole could be constrained to a more precise value, e.g., $M_{smbh} = (4.1 \pm 0.6) \cdot 10^6 M_\odot$ by Ghez et al. [38], however its influence on the fit is negligible, and its logarithm $\log(M_{smbh}/M_\odot) \sim 15.2$ comparing with our fit results 15.1 ± 0.2, 15.0 ± 0.3 is in the range of one standard deviation.

Appendix B. RDM model in strong fields

Here we reproduce the main results [1] on the structure of RDM solution in strong gravitational fields. The matter distribution, shown on Fig.4, in spherical coordinates (t, r, θ, ϕ) with a standard metric

$$ds^2 = -A(r)dt^2 + B(r)dr^2 + r^2(d\theta^2 + \sin^2\theta\, d\phi^2) \tag{B.1}$$

and a choice of energy-momentum tensor

$$T^{\mu\nu} = \rho_0(r)(u^\mu_+(r)u^\nu_+(r) + u^\mu_-(r)u^\nu_-(r)), \tag{B.2}$$

corresponding to the density $\rho_0(r)$ and velocity fields of T-symmetric outgoing/ingoing radial matter flows $u_\pm(r) = (\pm u^t(r), u^r(r), 0, 0)$, has a general analytic solution of geodesic equations in the form

$$4\pi\rho_0 = c_1/\left(r^2 u^r \sqrt{AB}\right),\ u^t = c_2/A,\ u^r = \sqrt{c_2^2 + c_3 A}/\sqrt{AB}. \tag{B.3}$$

Here $c_{1,2}$ are positive constants and $c_3 = u_\mu u^\mu$ takes three possible values $c_3 = -1, 0, 1$, dependently on the type of matter (massive, null or tachyonic). Restricting ourselves to $c_3 = 0$, null radial dark matter (NRDM), the remaining equations to solve are

$$da/dx = -1 + e^b + \epsilon\, e^{b-a},\ db/dx = 1 - e^b + \epsilon\, e^{b-a}, \tag{B.4}$$

written in logarithmic variables (29), with $\epsilon = 4c_1c_2$ and a starting point

$$x_1 = \log r_1,\ a_1 = 0,\ b_1 = \epsilon + r_s/r_1. \tag{B.5}$$

Here r_s is a gravitational radius of RDM-star and r_1 is the starting radius of the integration. This system is solved numerically, using Mathematica algorithm `NDSolve`. The result is presented on Fig.7 left.

Further, the density and radial pressure of dark matter, defined as energy-momentum tensor components $T^\mu_\nu = \mathrm{diag}(-\rho, p_r, 0, 0)$ are given by (31). Then, the Planck condition $\rho = l_P^{-2}$ in logarithmic variables has the form $a = \log(\epsilon l_P^2/(8\pi)) - 2x$. For the RDM solution with the MW galaxy parameters in the graph Fig.7 on the left, we get the intersection at

$$r_{QG} \sim r_s = 1.2 \cdot 10^{10}\mathrm{m},\ a_{QG} = -224.591,\ b_{QG} = -195.128, \tag{B.6}$$

$$A_{QG} = 2.89 \cdot 10^{-98},\ B_{QG} = 1.81 \cdot 10^{-85}. \tag{B.7}$$

Due to the proximity of r_{QG} and r_s, for the obtained value of A_{QG}, the formula (32) is valid with high accuracy. For the value of b_{QG}, the formula $b_{QG} = a_{QG} - 2\log\epsilon$ is also valid with high accuracy, that is

$$A_{QG} = (l_P/r_s)^2/(8\pi) \cdot \epsilon,\ B_{QG} = (l_P/r_s)^2/(8\pi)/\epsilon. \tag{B.8}$$

Note that according to estimates of [1], in the inflation area, $b = a + c_9$, $c_9 \sim -2\log\epsilon$ holds in the initial interval, in the leading order in ϵ. This relationship also holds, not only in order, but with high accuracy, in our numerical experiment with selected model constants. Another relation from [1], $b_2 = -a_2 - c_8$, describes a small deepening of the maximum of b_2 compared to Schwarzschild mode $b = -a$, which, apparently, is a local effect, not propagating in the adjacent asymptotics.

Another subtle effect is the small difference between the point r_2 and the nominal Schwarzschild radius r_s already noted in [1]. While the nominal radius is used in the formulation of the initial value b_1, at large distances, found by asymptotic formulas, the point r_2 corresponds to the maximum of the b -function located in the region of strong gravitational fields and found with an accurate account for all effects in the result of numerical integration. For the used parameters, r_2 is lower than r_s by 10%. Note that the value of r_s itself was reconstructed from the orbits of S-stars in [38] with an accuracy of about 10%. Therefore, this difference has no practical value, but we are interested in the principal question of the model calibration.

As noted in [1], other features of the gravitational field, such as the innermost stable circular orbit (ISCO), correspond to the value of r_2, rather than the nominal r_s, which means that in Schwarzschild mode, the r_2, not r_s, plays the role of a gravitational radius. We also calculated the orbital velocity using exact formulas from [1], $v^2 = da/dx/2$, for the position of S-stars $r \sim 2 \cdot 10^{13}$ m ... $3 \cdot 10^{14}$ m and found that the correspondence with the Newtonian approximation holds better for $v^2 = r_2/(2r)$ than for $v^2 = r_s/(2r)$.

Because of this, we recalibrated the model, selecting the nominal value of $r_{s,nom}$ so as to get $r_2 = r_{s,exp}$. The required nominal value turned out to be $r_{s,nom} = 1.32 \cdot 10^{10}$ m. With such a nominal value, integration was performed, the results of which were presented in Fig.7 on the left, and for which the cutoff point was obtained (B.6). In the formulas (32), (B.8), the experimental value of r_s is used, which coincides with r_2 as a result of recalibration.

Due to the fact that for the RDM model in the region of inflation, the metric coefficients are extremely small, a peculiar phenomenon of gravitational beaming arises. The displacement of a light particle in the radial direction $dt = (B/A)^{1/2} dr \sim dr/\epsilon$ requires much less time by the clock of the remote observer than the comparable $dr \sim rd\theta$ shift in the tangential direction $dt = A^{-1/2} rd\theta$. In particular, when choosing the parameters (B.7), to move the particle in the radial direction by $dr = 1$ m, 8ms is required, while to move the particle in the tangential direction by $rd\theta = 1$ m, one needs $2 \cdot 10^{40}$ s, which is 23 orders of magnitude greater than the age of the universe. Practically, this means that the particles do not move in the tangential direction, from the point of view of the remote observer, as long as the particles are located in the region of small values of the metric coefficient A.

Now let us estimate the overdensity conditions in the Planck core. Suppose the core is incompressible, with a constant density ρ, which corresponds to the effective density $\rho_X = \rho\,(1 - \rho/\rho_c)$, $\rho_c \sim \rho_P$. This effective density determines the Misner-Sharp mass: $M = 4\pi r_s^3 \rho_X/3 = r_s(1 - B_{QG}^{-1})/2$. Note that the small positive values of $0 < B_{QG} \ll 1$, which we obtain in the RDM model in the region of inflation, correspond to the large negative M, typical for the Planck star model. Substituting here the formula (B.8), we get $M \sim -4\pi\epsilon r_s^3/l_P^2$, whence $\rho_X \sim -3\epsilon/l_P^2$. If the excess is relatively small, $\Delta\rho = \rho - \rho_c \ll \rho_P$, we get $\Delta\rho/\rho_P \sim 3\epsilon$.

Appendix C. Evaluation of FRB characteristics

Let us determine the frequency distribution for the snowball effect described above. Considering the compound Y_n formed by the original N-particle and the excited X_n^*-particles sticking to it, and using the energy-momentum conservation laws, we get $E(Y_n) = E_N + nm_X$, $P(Y_n) = P_N$, $m(Y_n) = ((E_N + nm_X)^2 - P_N^2)^{1/2} = (m_N^2 + 2nm_X E_N + (nm_X)^2)^{1/2}$, where E, P, m denote energy, momentum and mass of the considered particles. The mass of the excited state is $m(X_n^*) = m(Y_n) - m(Y_{n-1})$. We consider the limit $E_N \gg m_X \gg m_N$. For the first state, $m(X_1^*) \sim (2m_X E_N)^{1/2}$. Further, for $1 \ll n \ll 2E_N/m_X$ in the expression for $m(Y_n)$, the term $2nm_X E_N$ prevails under the root, as a result we get $m(X_n^*) \sim m(X_1^*) n^{-1/2}/2$. The excitation energy that can be converted into photons is $E(X_n^*) = m(X_n^*) - m(X)$, in the considered limit $E(X_n^*) \sim m(X_n^*)$.

When $n \gg 2E_N/m_X$, the term $(nm_X)^2$ prevails in $m(Y_n)$, $m(X_n^*) \sim m_X$ results, there are practically no excitations, the snowball is stopped. Due to $m_X \ll m(X_1^*)$, as well as after accounting for superstrong redshifts, this limit is realized in the low-energy part of the spectrum outside the FRB detection range.

If we fix $n = 100$ and limit FRB observations to the frequency range $[\nu_{out}/10, \nu_{out}]$, the radiation energy in this region will be determined by $m(Y_n) = (2nm_X E_N)^{1/2} = 10E(X_1^*)$, which is a fraction of the total available energy $\eta_{spec} = 10E(X_1^*)/E_N = 10(2m_X/m_N)^{1/2} A_{QG}^{1/4} = 10(2\lambda_N/r_s)^{1/2}(\epsilon/(8\pi))^{1/4}$. The numerical value of the spectral efficiency for the chosen parameters is $\eta_{spec} \sim 5 \cdot 10^{-14}$.

The efficiency of the beam energy transfer compared to isotropic one for λ/D law is $\eta_{beam} = 4\pi/((\pi/4)(\lambda/D)^2) = 16D^2/\lambda^2$, for $D = 10$ km and the considered frequency range $\sim 10^{8\text{-}12}$. One can make this estimate somewhat more accurate, assuming that $D_0 = 10$ km, $m_0 = 10^{15}$ kg is used as the default parameters for the falling object. According to the NASA Asteroid Fact Sheet (https://nssdc.gsfc.nasa.gov/planetary/factsheet/asteroidfact.html), in the Solar System there are asteroids of size 0.1...1000 km and masses $10^{10\text{-}21}$ kg. Consider the other value of the diameter of D, assuming that the asteroid has the same density. The rest energy will increase by the factor $(D/D_0)^3$. Requiring that $(D/D_0)^3 \eta_{rec} \eta_{spec} \eta_{beam} = 1$, we get $D = 20...110$ km, an asteroid larger than the original D_0, for which an FRB with an isotropic energy m_0 will be observed, within the frames of the losses modeled here.

Note that these estimates are highly model dependent. The low-frequency components of the spectrum take up most of the energy and can be completely lost in noise due to the large scatter broadening discussed above, as well as other effects. In this case, the low value of η_{spec} is justified. However, other models may have a different spectral index, $E|dn/dE| \sim E^\alpha$. For example, for $\alpha > 0$, the spectrum is skewed to the higher frequencies, and the leakage to low frequencies can be neglected. The integral of this dependence between the frequencies $[\nu_{min}, \nu_{max}]$ is proportional to $(\nu_{max}^{\alpha+1} - \nu_{min}^{\alpha+1})/(\alpha+1)$, and already at $\alpha > -1$ the contribution of low frequencies to the integral can be neglected. For such models $\eta_{spec} \sim 1$. On the other hand, the assumption of radiation in the form of a narrow beam may also not be fulfilled if the object incident on the Planck core before goes through the phase of splitting and smearing in orbits around the RDM-star. In this case $\eta_{beam} \sim 1$.

References

[1] Klimenko S V, Nikitin I N and Nikitina L D 2017 Numerical solutions of Einstein field equations with radial dark matter *Int. J. Mod. Phys. C* **28** 1750096 (*Preprint* 1701.01569)
[2] Visser M, Barceló C, Liberati S and Sonego S 2008 Small, dark, and heavy: but is it a black hole? *Proc. of Science* **075** 010 (*Preprint* 0902.0346)
[3] Rubin V C and Ford W K Jr 1970 Rotation of the Andromeda Nebula from a spectroscopic survey of emission regions *ApJ* **159** 379-403
[4] Rubin V C, Ford W K Jr and Thonnard N 1978 Extended rotation curves of high-luminosity spiral galaxies *ApJ* **225** 107-111
[5] Ryabov V A, Tsarev V A and Tskhovrebov A M 2008 The search for dark matter particles, *Phys. Usp.* **51** 1091
[6] Persic M and Salucci P 1995 Rotation curves of 967 spiral galaxies *ApJ Supp.* **99** 501 (*Preprint* astro-ph/9502091)
[7] Persic M, Salucci P and Stel F 1996 Rotation curves of 967 spiral galaxies: Implications for dark matter *Astrophys. Lett. Comm.* **33** 205-211 (*Preprint* astro-ph/9503051)
[8] Persic M, Salucci P and Stel F 1996 The universal rotation curve of spiral galaxies: I. The dark matter connection *MNRAS* **281** 27-47 (*Preprint* astro-ph/9506004)
[9] Salucci P, Lapi A, Tonini C, Gentile G, Yegorova I and Klein U 2007 The universal rotation curve of spiral galaxies: II. The dark matter distribution out to the virial radius *MNRAS* **378** 41-47 (*Preprint* astro-ph/0703115)
[10] Karukes E V and Salucci P 2017 The universal rotation curve of dwarf disk galaxies *MNRAS* **465** 4703-4722 (*Preprint* 1609.06903)
[11] Sofue Y, Honma M and Omodaka T 2009 Unified rotation curve of the galaxy – decomposition into de Vaucouleurs bulge, disk, dark halo, and the 9-kpc rotation dip *Pub. Astron. Soc. Jap.* **61** 227-236 (*Preprint* 0811.0859)
[12] Sofue Y 2009 Pseudo rotation curve connecting the galaxy, dark halo, and local group *Pub. Astron. Soc. Jap.* **61** 153-161 (*Preprint* 0811.0860)
[13] Sofue Y 2012 A grand rotation curve and dark matter halo in the Milky Way galaxy *Pub. Astron. Soc. Jap.* **64** 75 (*Preprint* 1110.4431)
[14] Sofue Y 2013 Rotation curve and mass distribution in the galactic center – from black hole to entire galaxy *Pub. Astron. Soc. Jap.* **65** 118 (*Preprint* 1307.8241)
[15] Hamilton A J S and Pollack S E 2005 Inside charged black holes: II. Baryons plus dark matter *Phys. Rev. D* **71** 084032 (*Preprint* gr-qc/0411062)
[16] Rovelli C and Vidotto F 2014 Planck stars *Int. J. Mod. Phys. D* **23** 1442026 (*Preprint* 1401.6562)
[17] Barceló C, Carballo-Rubio R and Garay L J 2016 Black holes turn white fast, otherwise stay black: no half measures *J. High Energ. Phys.* 157 (*Preprint* 1511.00633)
[18] Petroff E, Barr E D, Jameson A, Keane E F, Bailes M, Kramer M, Morello V, Tabbara D and van Straten W 2016 FRBCAT: The fast radio burst catalogue *Pub. Astron. Soc. Australia* **33** e045 (*Preprint* 1601.03547)
[19] Platts E, Weltman A, Walters A, Tendulkar S P, Gordin J E B and Kandhai S 2019 A living theory catalogue for fast radio bursts *Phys. Rep.* **821** 1-27 (*Preprint* 1810.05836)
[20] Kirillov A A 1999 Effects related to spacetime foam in particle physics *Sov. Phys. JETP* **88** 1051-1057 (*Preprint* hep-th/9911168)
[21] Kirillov A A 2002 Dark matter, dark charge, and the fractal structure of the universe *Phys. Lett. B* **535** 22 (*Preprint* astro-ph/0203267)
[22] Kirillov A A 2003 Violation of the Pauli principle and dimension of the universe at very large distances *Phys. Lett. B* **555** 13 (*Preprint* astro-ph/0211162)
[23] Kirillov A A 2006 The nature of dark matter *Phys. Lett. B* **632** 453 (*Preprint* astro-ph/0505131)
[24] Kirillov A A and Turaev D 2002 On modification of the Newton's law of gravity at very large distances *Phys. Lett. B* **532** 185 (*Preprint* astro-ph/0202302)
[25] Kirillov A A and Turaev D 2006 The universal rotation curve of spiral galaxies *MNRAS* **371** L31-L35 (*Preprint* astro-ph/0604496)
[26] Freeman K C 1970 On the disks of spiral and S0 galaxies *ApJ* **160** 811
[27] Andreon S 2010 The stellar mass fraction and baryon content of galaxy clusters and groups *MNRAS* **407** 263 (*Preprint* 1004.2785)
[28] WMAP Science Team (Dunkley J et al) 2009 Five-year Wilkinson microwave anisotropy probe (WMAP) observations: likelihoods and parameters from the WMAP data *ApJ Suppl.* **180** 306-329 (*Preprint* 0803.0586)
[29] Planck Collaboration (Aghanim N et al) 2018 Planck 2018 results. VI. Cosmological parameters *Preprint* 1807.06209

[30] Blau M 2018 *Lecture Notes on General Relativity* (University of Bern)
[31] Merritt D, Graham A W, Moore B, Diemand J and Terzic B 2006 Empirical models for dark matter halos. I. Nonparametric construction of density profiles and comparison with parametric models *Astron. J.* **132** 2685-2700 (*Preprint* astro-ph/0509417)
[32] Barranco J, Bernal A and Nunez D 2015 Dark matter equation of state from rotational curves of galaxies *MNRAS* **449** 403 (*Preprint* 1301.6785)
[33] Ashtekar A, Pawlowski T and Singh P 2006 Quantum nature of the Big Bang *Phys. Rev. Lett.* **96** 141301 (*Preprint* gr-qc/0602086)
[34] Ashtekar A, Pawlowski T and Singh P 2006 Quantum nature of the Big Bang: an analytical and numerical investigation *Phys. Rev. D* **73** 124038 (*Preprint* gr-qc/0604013)
[35] Ashtekar A, Pawlowski T and Singh P 2006 Quantum Nature of the Big Bang: improved dynamics *Phys. Rev. D* **74** 084003 (*Preprint* gr-qc/0607039)
[36] Cao X F, Xiao M and Xiao F 2017 Modeling the redshift and energy distributions of fast radio bursts *Res. Astron. Astrophys.* **17** 14
[37] Sofue Y and Rubin V C 2001 Rotation curves of spiral galaxies *Ann. Rev. Astron. Astrophys.* **39** 137-174 (*Preprint* astro-ph/0010594)
[38] Ghez A M et al 2008 Measuring distance and properties of the Milky Way's central supermassive black hole with stellar orbits *ApJ* **689** 1044-1062 (*Preprint* 0808.2870)
[39] Fedorova V and Rodin A 2019 Detection of fast radio bursts on the Large Scanning Antenna of the Lebedev Physical Institute *Astron. Rep.* **63** 39-48 (*Preprint* 1812.10716)
[40] Spitler L et al 2016 A repeating fast radio burst *Nature* **531** 202-205 (*Preprint* 1603.00581)
[41] Scholz P et al 2016 The repeating fast radio burst FRB 121102: multi-wavelength observations and additional bursts *ApJ* **833** 177 (*Preprint* 1603.08880)
[42] Gajjar V et al 2018 Highest frequency detection of FRB 121102 at 4-8 GHz using the Breakthrough Listen digital backend at the Green Bank Telescope *ApJ* **863** 2 (*Preprint* 1804.04101)
[43] Zhang Y G, Gajjar V, Foster G, Siemion A, Cordes J, Law C and Wang Y 2018 Fast radio burst 121102 pulse detection and periodicity: a machine learning approach *ApJ* **866** 149 (*Preprint* 1809.03043)
[44] Hessels J W T et al 2019 FRB 121102 Bursts Show Complex Time-Frequency Structure *ApJL* **876** L23 (*Preprint* 1811.10748)
[45] Houde M, Mathews A and Rajabi F 2017 Explaining fast radio bursts through Dicke's superradiance *MNRAS* **475** 514 (*Preprint* 1710.00401)
[46] Waxman E 2017 On the origin of fast radio bursts *ApJ* **842** 34 (*Preprint* 1703.06723)
[47] Diels J C and Rudolph W 2006 *Ultrashort Laser Pulse Phenomena* (New York: Academic)
[48] Lorimer D R, Bailes M, McLaughlin M A, Narkevic D J and Crawford F 2007 A bright millisecond radio burst of extragalactic origin *Science* **318** 777 (*Preprint* 0709.4301)
[49] Luan J and Goldreich P 2014 Physical constraints on fast radio bursts *ApJL* **785** L26 (*Preprint* 1401.1795)
[50] Ravi V, Shannon R M and Jameson A 2015 A fast radio burst in the direction of the Carina dwarf spheroidal galaxy *ApJL* **799** L5 (*Preprint* 1412.1599)
[51] Burke-Spolaor S and Bannister K W 2014 The galactic position dependence of fast radio bursts and the discovery of FRB011025 *ApJ* **792** 19 (*Preprint* 1407.0400)
[52] Masui K et al 2015 Dense magnetized plasma associated with a fast radio burst *Nature* **528** 523-525 (*Preprint* 1512.00529)
[53] Prochaska J X and Neeleman M 2018 The astrophysical consequences of intervening galaxy gas on fast radio bursts *MNRAS* **474** 318-325 (*Preprint* 1711.00323)
[54] Xu S and Zhang B 2016 On the origin of the scatter broadening of fast radio burst pulses and astrophysical implications *ApJ* **832** 199 (*Preprint* 1608.03930)
[55] Thornton D et al 2013 A population of fast radio bursts at cosmological distances *Science* **341** 53-56 (*Preprint* 1307.1628)
[56] Dai Z G, Wang J S, Wu X F and Huang Y F 2016 Repeating fast radio bursts from highly magnetized pulsars travelling through asteroid belts *ApJ* **829** 27 (*Preprint* 1603.08207)
[57] Lu W, Kumar P and Narayan R 2019 Fast radio burst source properties from polarization measurements *MNRAS* **483** 359-369 (*Preprint* 1810.09459)
[58] Suresh A and Cordes J M 2019 Induced polarization from birefringent pulse splitting in magnetoionic media *ApJ* **870** 29 (*Preprint* 1808.09471)
[59] Katz J I 2018 FRB sky distribution, rarity, energetics, magnetic reconnection and sources *Preprint* 1811.10755
[60] Wheeler J C and Johnson V 2011 Stellar mass black holes in young galaxies *ApJ* **738** 163 (*Preprint* 1107.3165)